

Elasticity in the skyrmion phase unveils depinning at ultra-low current densities

Yongkang Luo^{1,*}, Shizeng Lin¹, M. Leroux¹, N. Wakeham¹, D. M. Fobes¹, E. D. Bauer¹,
J. B. Betts¹, J. D. Thompson¹, A. Migliori¹, M. Janoschek¹, and Boris Maiorov^{1†}
¹ *Los Alamos National Laboratory, Los Alamos, New Mexico 87545, USA.*

(Dated: November 27, 2017)

Controlled movement of nano-scale stable magnetic objects has been proposed as the foundation for a new generation of magnetic storage devices. Magnetic skyrmions, vortex-like spin textures stabilized by their topology are particularly promising candidates for this technology. Their nanometric size and ability to be displaced in response to an electrical current density several orders of magnitude lower than required to induce motion of magnetic domain walls suggest their potential for high-density memory devices that can be operated at low power. However, to achieve this, skyrmion movement needs to be controlled, where a key question concerns the coupling of skyrmions with the underlying atomic lattice and disorder (pinning). Here, we use Resonant Ultrasound Spectroscopy (RUS), a probe highly sensitive to changes in the elastic properties, to shed new light on skyrmion elasticity and depinning in the archetypal skyrmion material MnSi. In MnSi, skyrmions form a lattice that leads to pronounced changes in the elastic properties of the atomic lattice as a result of magneto-crystalline coupling. Without an applied current, the shear and compressional moduli of the underlying crystal lattice exhibit an abrupt change in the field-temperature range where skyrmions form. For current densities exceeding j_c^* the changes of elastic properties vanish, signaling the decoupling of skyrmion and atomic lattices. Interestingly, j_c^* , which we identify as the onset of skyrmion depinning, is about 20 times smaller than j_c previously measured via non-linear Hall effect. Our results suggest the presence of a previously-undetected intermediate dynamic regime possibly dominated by skyrmion-creep motion with important consequences for potential applications.

I. INTRODUCTION

Magnetic skyrmions are topologically-stabilized objects with a whirl-like spin-texture that emerges from a magnetic field- and temperature-tuned balance of magnetic interactions[1]. Their response to electrical currents as well as their nanoscale size make them highly promising for applications in spintronics and memory devices[2, 3]. Because of their topological properties, they pin weakly to the underlying atomic lattice and defects. This results in critical current densities required to induce skyrmion motion that are ultra-low compared to currents typically necessary to produce current-driven magnetization dynamics in magnetic domains, making them, among others, prime candidates for so-called race-track memory devices. All proposed devices architectures require a detailed understanding of skyrmion pinning and in some cases on being able to engineer appropriate pinning landscapes to control skyrmion movement.

In bulk materials, a single skyrmion is a line-like structure oriented parallel to an external magnetic field (\mathbf{H}) [see Fig. 1(a)] and in this sense is qualitatively analogous to vortices of magnetic flux that form in a superconductor subject to an applied magnetic field. Moreover, skyrmion lines also form a hexagonal skyrmion lattice (SKX) due to repulsive interactions and can be moved in response to an electromotive force sufficiently large to depin them from the disorder present in the sample. Because of these similarities, it is tempting to apply to skyrmions certain pinning models developed for superconducting vortices[4]. The depinning current density for a skyrmion lattice in single crystals is low, indicating weak pinning, and re-

sults of previous studies have been successfully related to a weak collective pinning model[5, 6]. In this model, the critical current which sets the onset of movement is determined by a trade-off between the strength of the pinning potential and the elastic stiffness of the lattice[4]. This critical current depends *inversely* on the lattice stiffness, meaning that a perfectly rigid lattice of linear objects like vortices or skyrmions cannot be pinned[4].

Theoretically, however, the interaction between pinning centers and skyrmions differs from superconducting vortices, notably because skyrmion motion is dominated by a large Magnus force that tends to scatter skyrmions with a velocity perpendicular to the pinning force. This allows skyrmions to avoid passing through the pinning centers in contrast to vortices for which the Magnus force can be disregarded[7]. Thus, for example, skyrmions that depin because of thermal fluctuations cannot be easily recaptured by pinning centers, making pinning of skyrmions less effective compared to vortices[7].

Microscopically, skyrmion movement has been investigated directly through Lorentz Transmission Electron Microscopy (LTEM)[8] and by the spin-transfer torque over the lattice seen by small-angle neutron scattering (SANS)[5]. Macroscopically, it has also been inferred from a reduction of the topological Hall effect (THE) at large current densities[9, 10]. However, apart from the associated macroscopic critical current density, j_c , no detailed experimental information on the depinning process is available, and it remains unknown how and which material defects affect skyrmions and to what extent their spin influences pinning[7].

We exploit this magneto-crystalline coupling by us-

ing Resonant Ultrasound Spectroscopy (RUS) measurements to determine with unprecedented resolution the elastic response of the atomic lattice to the formation and depinning of the skyrmion lattice in the prototypical skyrmion lattice material MnSi. From the changes of the measured bulk elastic properties, we can infer the skyrmion lattice elastic properties and detect depinning of skyrmions. Quantitative values of SKX elasticity are useful in constructing an effective skyrmion pinning theory, and determining the relevant parameters needed for successful pinning models. Previous ultrasound measurements on MnSi and related MnGe based on a pulse-echo technique have already demonstrated the sensitivity to the presence of the SKX as a consequence of its coupling to the crystalline lattice, revealing diverse behavior depending on the type of skyrmion lattice (MnSi, MnGe etc)[11–13]. Skyrmion lattice stiffness was estimated to be 3 orders of magnitude smaller than that of the atomic lattice of MnSi, being as soft as the vortex lattice in superconductors[11]. The relative small variation in elastic constants, permits the use of the changes in bulk stiffness as a measure of the skyrmion lattice stiffness, at least as a first order[11].

Compared to pulsed-echo measurements, RUS used here has significant advantages; RUS determines the complete elastic tensor in a single measurement with no transducer-sample bond[14, 15]. By measuring all the elastic moduli C_{ij} *simultaneously* with a fixed magnetic field orientation, accounting for anisotropic demagnetization factors is unnecessary and direct comparisons among C_{ij} can be made. In contrast, pulse-echo studies require different samples or rotating the sample with respect to the magnetic field to obtain the complete elastic tensor[11, 13].

Our RUS measurements reveal the complete elastic tensor (six independent irreducible moduli C_{ij}) of a single crystal of MnSi and the coupling of the SKX to the bulk elastic response of the atomic lattice. Upon entering the skyrmion phase, we find a much smaller response for shear than for compressional moduli, confirming a similarity with superconducting vortex lattices[4]. Applying current, we identify the elastic response related to the decoupling of the SKX above a critical current density j_c^* . We determine the temperature dependence of j_c^* and compare it to the thermodynamic stiffness variation associated with the skyrmion lattice measured with zero current applied, determining the limits of applicability of the weak collective pinning model. The value of j_c^* is ~ 20 times smaller than the critical current density j_c measured by changes in THE and SANS[5, 9]. Our work identifies j_c^* is the onset of skyrmion movement, and that the differences in magnitude and temperature dependence with respect to j_c suggests the presence of an intermediate dynamic regime dominated by SKX creep motion that was previously undetected.

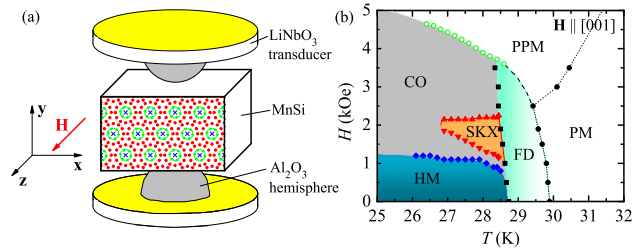


FIG. 1. (a) Schematic diagram of the RUS experimental setup. (b) RUS magnetic phase diagram. The open circles are from $\chi'(H)$, defined as the mid-point of spin polarization. The abbreviations denoting the different phases are: HM = helimagnetic, CO = conical, SKX = skyrmion lattice, FD = fluctuation disordered, PM = paramagnetic, and PPM = polarized paramagnetic.

II. EXPERIMENTAL DETAILS

The MnSi single crystal was grown by the Bridgman-Stockbarger method followed by a 1-week anneal at 900°C in vacuum. The stoichiometry ratio of Mn:Si=0.88:1.12 was estimated by energy dispersive x-ray spectroscopy (EDS). The sample was polished into a parallelepiped along the [001] direction with dimensions $1.446 \times 0.485 \times 0.767$ mm³. The orientation of the crystal was verified by Laue X-ray diffraction within 1°. Electrical resistivity and AC susceptibility measurements revealed a magnetic transition as expected at $T_c=28.7$ K, and a residual resistance ratio $RRR[\equiv \rho(300\text{ K})/\rho(2\text{ K})]=87$, indicating a high quality single crystal [See Fig. S1 in **Supporting information (SI)**]. All the measurements in this work were performed on the same crystal. Further, the SKX in a different piece of this sample was directly observed using SANS[27].

A schematic diagram of the RUS setup is shown in Fig. 1(a). The sample was mounted between two LiNbO₃ transducers. In order to stabilize the sample in a magnetic field and maintain RUS-required weak transducer contact, Al₂O₃ hemispheres (that also act as wear plates and electrical insulators) were bonded to each transducer. The external magnetic field \mathbf{H} was applied along [001] of the cubic crystal structure of MnSi. Frequency sweeps from 1250 to 5300 kHz were performed for each measurement. The resonance peaks were tracked and recorded as a function of temperature and magnetic field. Elastic moduli C_{ij} were extracted from 24 resonance frequencies with an RMS error of 0.2% using an inversion algorithm[14, 15]. Although the absolute error is large (mainly because of uncertainties in the sample dimensions), the precision of the elastic moduli determination is at least 1×10^{-7} .

To study the effect of current on moduli, we attached gold wires (13 μm) at opposite sides of the specimen allowing a DC current to be applied along [100], $\mathbf{L}\perp\mathbf{H}$ with a cross-section of $0.485\times 0.767\text{ mm}^2$. To minimize Joule heating at the contacts, the Au wires were spot-welded to the sample and covered with silver paint to improve current homogeneity and reduce contact resistance. The resulting Ohmic electrical contacts were less than $0.5\ \Omega$. Whenever the current was changed, we waited for steady state before recording. A small temperature increase ($<30\text{ mK}$) was observed at the thermometer right after applying relatively larger currents. We compensated for this by adjusting the set-point of the temperature controller.

III. RESULTS AND DISCUSSIONS

In this section, we describe the response of the elastic moduli to the formation of the SKX as a function of temperature (T) and magnetic field (H). In addition, we also explore the change of the elastic properties when electrical currents of density j are applied to induce motion of the SKX. We use the extreme sensitivity of RUS to detect all relevant magnetic phase transitions, and the symmetry sensitivity of RUS to understand the observations. We reveal the envelope of skyrmion depinning, analyze the temperature dependence of critical depinning current j_c^* in the framework of a weak collective pinning model, and provide insight into magneto-elastic coupling in this system.

Elastic moduli are thermodynamic susceptibilities that, when magneto-elastic coupling is important, are particularly favorable for observing phase boundaries. Details of the data analysis are described in **SI**. Figure 1(b) illustrates the magnetic phase diagram obtained via the elastic moduli and supported by magnetic susceptibility measurements. Both give results in good agreement with the literature[1] where the SKX phase appears in a narrow range of temperatures and field within the conically (CO) ordered magnetic phase. Figures 2(a-c) show the temperature dependencies of C_{ij} of MnSi for $H=0$ that we used to define the phase boundaries. For the cubic symmetry of MnSi and in the absence of a magnetic field, only three independent elastic moduli are required. Here we follow the tradition of using C_{11} , C_{12} and C_{44} as the independent elastic moduli (**SI**). In addition, the [110] shear modulus is defined as $C^*\equiv(C_{11}-C_{12})/2$. At room temperature, we find $C_{11}=316.54\text{ GPa}$, $C_{12}=86.96\text{ GPa}$, and $C_{44}=121.53\text{ GPa}$ in good agreement with the literature[13]. Upon cooling, both C_{11} and C_{44} increase. As temperature is lowered below 35 K, C_{11} and C_{44} drop but C^* rises. This is characteristic of softening in one symmetry direction and stiffening in another in the vicinity of the magnetic phase transition to the helimagnetic (HM) state, highlighting

the importance of measuring the full elastic tensor. The change of C_{44} and C^* are much smaller than those of C_{11} and C_{12} . C_{11} exhibits a minimum at $T^*=29.8\text{ K}$ before recovering and then displaying an inflection at $T_c=28.7\text{ K}$ where the system undergoes a PM-HM (helimagnetic) transition. The derived T_c agrees well with AC susceptibility measurements shown in the right inset to Fig. 2(b). In the low temperature limit, all C_{ij} tend to saturate, as expected. It should be mentioned that T^* is about 1 K above T_c , corresponding to a so-called Vollhardt invariance previously determined via specific heat and neutron scattering measurements[16, 17]. Notably, T^* is a characteristic temperature that describes a crossover from mean-field ferromagnetic to strongly-interacting HM fluctuations. Thus, the window between T^* and T_c describes the fluctuation-disordered (FD) region on the phase diagram [Fig. 1(b)], where strong critical fluctuations of the helical order parameter reduce both the correlation length and the mean-field helical phase transition temperature, resulting in a Brazovskii-type first-order transition at T_c [17, 18].

In the presence of a magnetic field $\mathbf{H}\parallel[001]$, symmetry is broken and the \mathbf{z} -axis is no longer equivalent to the \mathbf{x} - and \mathbf{y} -axes. This lowers the symmetry of the elastic tensor from cubic to tetragonal (**SI**), requiring three additional independent elastic moduli, C_{33} , $C_{23}(=C_{31})$ and C_{66} . In Figs. 2(e-g), we plot C_{ij} as a function of H at $T=28\text{ K}$. Each subset of C_{ij} splits into two branches under magnetic field. By extracting the six C_{ij} from the same frequency scan, we are able to track all the moduli as a function of field and observe a discontinuous jump in some C_{ij} between $H_{a1}=1.4\text{ kOe}$ and $H_{a2}=2.2\text{ kOe}$. Based on the field dependence of χ' shown in Fig. S2(b) (**SI**), we determine H_{a1} and H_{a2} as the lower and upper boundaries of the SKX phase, respectively. Below H_{a1} , there is a weak inflection in $C_{ij}(H)$ near $H_{c1}=1.0\text{ kOe}$, which we assign to the field-induced helimagnetic (HM)-conical (CO) phase transition. A closer look at Figs. 2(e-g) reveals contrasting behavior for different C_{ij} . Although both compression (C_{11} , C_{33}) and shear moduli (C_{44} , C_{66}) display abrupt changes, C_{12} and C_{23} only exhibit a slight change in slope near H_{a1} and H_{a2} . The amplitudes of the elastic moduli jumps are consistent with what was measured previously[11, 13]. A much smaller variation is found in the shear than in the compression moduli, being 3×10^{-5} and $1.5\times 10^{-3}\text{ GPa}$ respectively [see Figs. 2(e,f)]. It is important to remember that we are measuring the elastic moduli of the entire crystal and although the changes are associated with the existence and properties of the SKX, the detected signal is characteristic of the SKX coupled to the overall sample elasticity. Looking at C^* in Fig. 2(h), the jump is an order of magnitude bigger than that found for C_{66} , indicating that hexagonal symmetry of the SKX does not describe the system, as for this we would expect $C^*=C_{66}$ (**SI**). Thus, tetragonal symmetry resulting from applying a magnetic

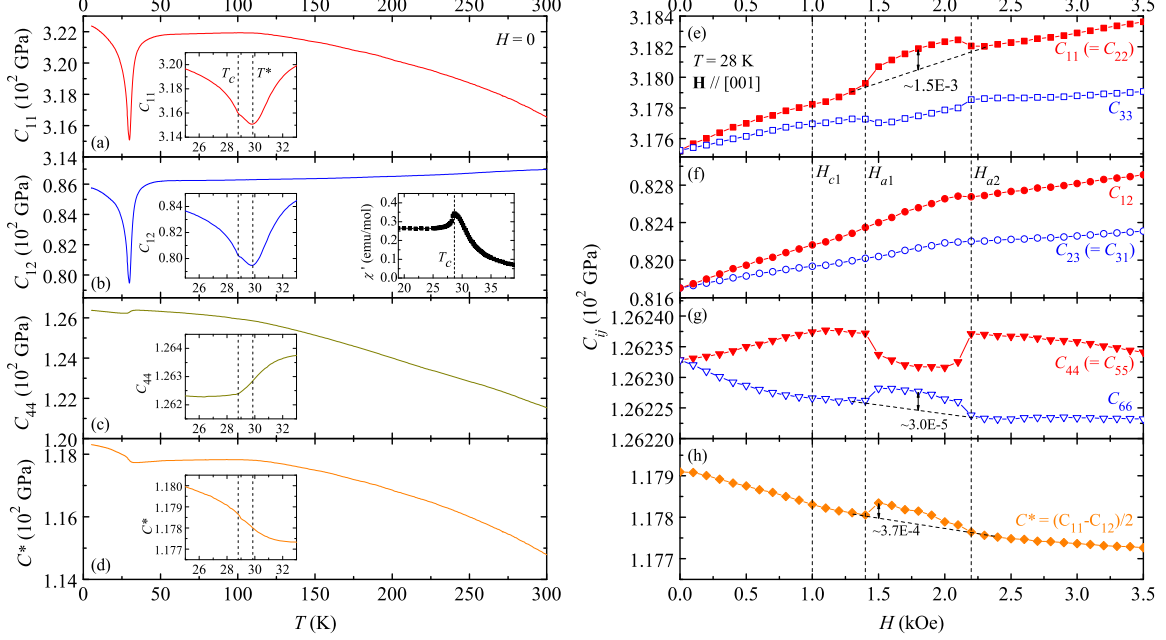


FIG. 2. Temperature dependence of elastic moduli of MnSi. (a-d) Zero-field temperature dependence of C_{11} , C_{12} , C_{44} and $C^* \equiv (C_{11} - C_{12})/2$, respectively. The insets are near $T_c = 28.7$ K. The right inset to panel (b) displays the real part of AC susceptibility χ' as a function of T . (e-h) Isothermal field dependent C_{ij} at $T = 28$ K.

field to the cubic system is the appropriate symmetry to consider for this system.

Because we have computed the contribution of each elastic moduli to each resonance frequency, it is useful and more precise to plot the raw frequencies when only trends and discontinuities are sought[19]. Table S1 in SI shows the resulting least-square-fitting for C_{ij} measured at $T = 34$ K and $H = 0$. The dependence of each resonance frequency on each C_{ij} , i.e. $\partial F / \partial C_{ij}$, is presented (normalized) and shown in the last nine columns of the table. Because the third and fourth frequencies in the table depend predominantly on C_{11} , we can use these resonances, F_{1654} and F_{2419} , as a simpler measure of C_{11} . For a frequency that depends only on one C_{ij} we have $C_{ij} \propto F^2$, so for small changes of those C_{ij} we have $\delta C_{ij} \sim 2\delta F$.

Using only resonance frequencies, Fig. 3(a) displays the temperature dependence of the relevant elastic moduli at various magnetic fields. For $H = 0$, the behavior of $F_{2419}(T)$ resembles that of $C_{11}(T)$, confirming the dominance of C_{11} . With increasing magnetic field, T_c is gradually suppressed, and the signature of the phase transition becomes more pronounced for $H > 2.5$ kOe. The temperature where minimum of $F_{2419}(T)$ occurs initially decreases with increasing H but then broadens and shifts to higher T for $H > 2.5$ kOe where spins become polarized by the external field. Figure 3(b) shows F_{1654} as a function of H measured at selected temperatures. The discontinuous jump in $F_{1654}(H)$ can be identified between

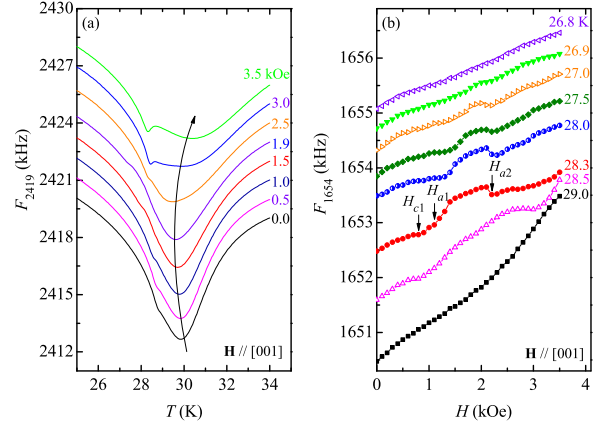


FIG. 3. Two representative RUS resonance-peak frequencies dominated by C_{11} . The curves are vertically shifted for clarity. (a) Temperature dependence of F_{2419} at different fields. The arrow marks the evolution of the minimum of F_{2419} with field. (b) Field dependence of F_{1654} at various temperatures. Arrows mark characteristic fields corresponding to phase transitions.

26.9 K and 28.5 K similarly as seen in C_{11} in Fig. 2(b). A positive jump in $F_{1654}(H)$ signifies stiffening in C_{11} when the system enters the SKX phase. The magnitude of the

jump in $F_{1654}(H)$, denoted by ΔF , is plotted as a function of temperature in Fig. 4(g) with a maximum near the SKX-FD boundary and decreasing as T decreases. The value of ΔF can be regarded as a measure of convolution between the SKX lattice stiffness and the strength of the coupling between SKX and the atomic lattice. Indeed, the maximum in ΔF near the upper boundary of the SKX ($T \sim 28.2$ K) phase can be explained by proximity to the fluctuation disordered regime; the abundance of critical magnetic fluctuations makes the skyrmion lattice softer, which would allow for better pinning to material disorder (see below).

Electrical current also influences elastic properties of the atomic lattice in the SKX phase. Figures 4(a-d) display the field dependence of F_{1654} with various applied electrical currents ($\mathbf{I} \perp \mathbf{H}$) at four selected temperatures 28.4, 28.2, 27.7 and 27.1 K inside the SKX phase, respectively. Taking $T=27.7$ K as an example (Fig. 4c), we subtract a smooth background $F_{bkg}(H)$ from the raw $F_{1654}(H)$, the results of which are shown in [Fig. 4(e)]. ΔF is then defined as the maximum of $F_{1654} - F_{bkg}$. ΔF remains essentially unchanged for current values up to 21 mA, drops abruptly between 22 and 24 mA, and becomes nearly unresolvable at 25 mA. The threshold current density j_c^* is defined as the midpoint of the drop in ΔF , shown in Fig. 4(f) with $j_c^* = 62(3)$ kA/m² for 27.7 K. The error bar is set by the step size in current. In Fig. 4(f) we also show $\Delta F(j)$ for 27.1 K, and the difference in j_c^* s is far larger than the measurement uncertainty. The $F_{1654}(H)$ curves for $j > j_c^*$ do not display the characteristic stiffening signature corresponding to the skyrmion phase, as if the SKX is completely decoupled from the lattice.

We emphasize that the changes observed in the resonance frequencies are not caused by current-induced Joule heating as can be illustrated by several observations. (i) The magnitude of ΔF should increase with j [cf Fig. 4(f)] for temperatures near the lower boundary of the SKX phase (e.g. 27.1 K). (ii) j_c^* should increase monotonically with decreasing temperature. (iii) For significant Joule heating, the first point in Fig. 4(g), $T=26.8$ K below the skyrmion phase boundary, should display a non-zero ΔF , in contrast to what it is measured. (iv) The phase boundaries in H depend strongly on temperature as revealed in the phase diagram in Fig. 1(b). The width of the SKX phase with respect to field showing non-zero ΔF remains unaffected for increasing current density at all measured temperatures, as expected for constant temperature [Figs. 4(a-e)]. All these observations demonstrate that the coupling between the SKX and the crystals is lost at j_c^* .

The drastic changes in the elastic properties above j_c^* recall the measurements of the critical current for the onset of the skyrmion movement[5, 6, 8, 10]. However, the critical current $j_c \sim 1$ MA/m² derived from the decrease in the Hall signature[6], which has been associated with the

onset of movement of skyrmions caused by spin-torque[5], is about 20 times larger than our RUS results display.

There are several scenarios that can explain the difference in values between j_c and j_c^* . First, the presence of ultrasonic waves could facilitate depinning by shaking skyrmions off pinning potentials resulting in a smaller current for motion threshold. Such kind of j_c decrease was observed in other pinned systems like superconducting vortices[21] and recently in MnSi when applying an alternating magnetic field[22]. However, this effect is unlikely here because the same j_c^* is observed with ultrasonic excitations increased by a factor of 2 [full symbols in Fig. 4(g)].

Another possibility is that the disorder is lower or of a different kind compared to the crystals used for previous studies, which would yield a lower j_c in our sample. Because the RRR of our sample is comparable to that of previous studies, disorder density seems unlikely to be the cause of the smaller j_c observed here. However, the amount of disorder is not the only variable affecting skyrmion pinning (and order parameter); notably, the type, spin and valence of the defects need to be taken into account. Numerical simulations have shown that different types of defects may act as pinning or depinning centers depending on their nature[7, 23]. In this context, we find that our single crystals exhibit a slight Mn deficiency as verified by EDS (**SI**). This is also reflected in measurable differences between the MnSi crystal studied here and those used for previous Hall effect studies. For example the T_c here is about 0.5 K higher, and the Hall effect measured on several of our single crystals (including a slice taken from the same batch of the RUS sample) also shows differences, the details of which, will be part of a future publication. This points to a situation where the type of disorder present in our sample allows for more efficient SKX depinning.

We also consider the different sensitivities for detecting the onset of skyrmion motion using diverse techniques. For Hall effect measurements, j_c can only be identified after the motion of skyrmions produces a measurable change in the small THE. The situation in SANS is similar, as the resolution in reciprocal space will be limited if the skyrmions moves too slowly. In contrast, RUS directly measures the magneto-crystalline coupling, and thus detects skyrmion movement immediately when the SKX decouples (and hence a lower j_c). Therefore, RUS is similar to LTEM experiments which detect ON-OFF movement. This scenario is supported by the contrasting current dependence between RUS and Hall effect responses used to determine j_c . The abrupt change in ΔF as j reaches j_c^* is distinct from the gradual decrease of the topological Hall resistivity for $j > j_c$ [6].

A similar disparity occurs in detecting the critical current for superconducting vortex movement, in which j_c values determined from magnetization measurements are lower than those extracted using transport. The for-

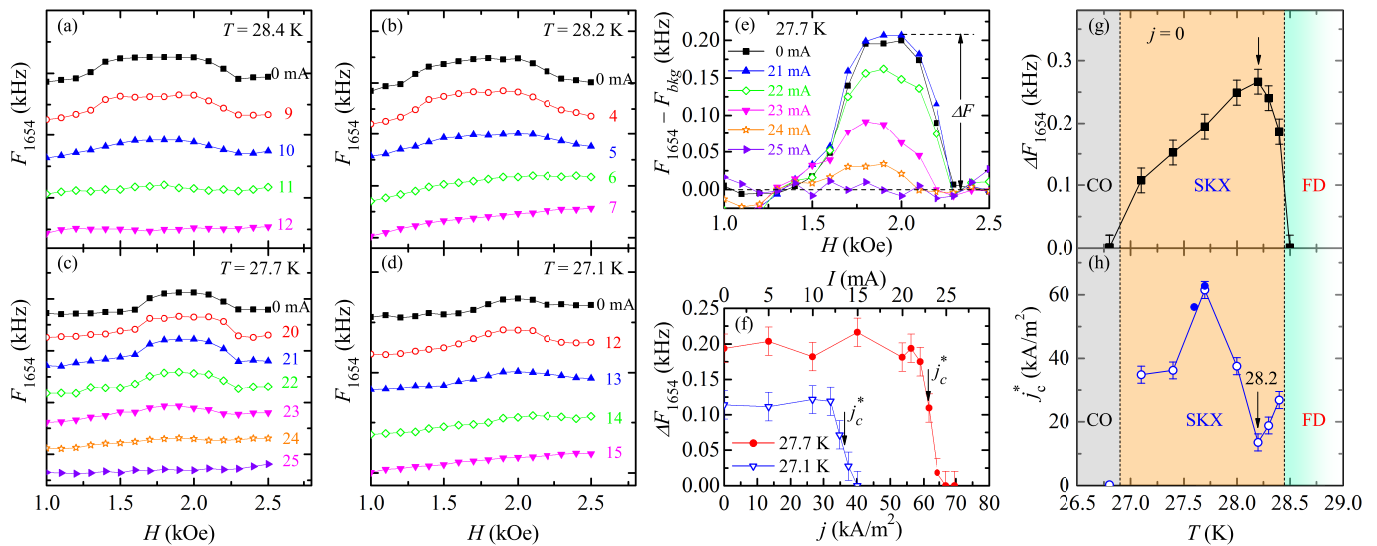


FIG. 4. Effect of applied current on F_{1654} . (a-d) Field dependence of F_{1654} at various currents, measured at 28.4 K, 28.2 K, 27.7 K and 27.1 K, respectively. The curves are vertically offset. (e) $F_{1654} - F_{bkg}$ as a function of H at 27.7 K, where F_{bkg} is the smooth background of F_{1654} . ΔF is defined as the maximum of $F_{1654} - F_{bkg}$. (f) ΔF_{1654} vs. j for 27.7 K and 27.1 K. The arrows mark the critical current density values $j_c^* = 62$ and 35 kA/m², respectively. (g) ΔF_{1654} as a function of T when in the absence of current. (h) temperature dependent j_c^* . The full symbols are measured with and ultrasonic excitation two time larger than that used to measured the open symbols.

mer are sensitive to creep and the latter to flux-flow changes[4, 24, 25]. It is likely that the situation here is similar, where the differing temperature dependences observed for j_c and j_c^* suggest that RUS and the Hall effect sense different dynamic regimes. As skyrmion movement is dominated by the Magnus force, this allows thermal fluctuations to depin the SKX with ease. Notably, the escape rate due to thermal fluctuations is proportional to $e^{(-\Delta U/k_B T)}$, where ΔU is the height of the pinning potential[7]. However, the applied current may not be sufficient to induce direct movements of the SKX, but driven creep motion would dominate this intermediate dynamic regime. We note that neither Hall effect nor SANS measurements are sensitive to such incoherent SKX motion.

Finally, the temperature dependence of j_c^* [Fig. 4(h)] provides additional important insight into skyrmion pinning. According to the weak collective pinning theory, j_c^* is inversely proportional to the SKX stiffness. The temperature dependence of $\Delta F(j=0)$ [see Fig. 4(g)] displays two trends. Starting at high temperature from the SKX-FD, ΔF increases as T decreases becoming stiffer down to $T=28.2$ K marked with a vertical arrow in Fig. 4(g). In agreement with weak collective pinning theory, we observe that j_c^* decreases and shows a minimum at $T=28.2$ K [vertical arrow in Fig. 4(h)]. The behavior for $T > 28.2$ K, is consistent with strong thermal fluctuations near the upper boundary of the SKX phase that soften the SKX lattice and allows skyrmion lines to accommodate better to disorder, improving pinning with the consequent

higher j_c^* . The increase in j_c^* near the SKX-FD phase boundary is called peak effect and was also observed in MnSi via the THE[6] and is ubiquitous to superconducting vortices in a weak pinning landscape[4, 26]. As T continues to decrease, j_c^* and $\Delta F(j=0)$ keep displaying an inverse relation consistent with a weak collective pinning down to $T=27.7$ K where j_c^* shows a maximum but ΔF only a weak inflection point. This temperature marks a change in pinning regime, indicating weak collective pinning is no longer valid below $T=27.7$ K. At lower temperatures j_c^* decreases and then remains constant. No signature of a peak effect was observed near the lower-temperature phase boundary because the low temperature CO-SKX phase transition is not fluctuation dominated as is the SKX-FD. The non-monotonic $j_c^*(T)$ indicates that there are more than one pinning regimes.

IV. CONCLUSIONS

In summary, we have determined the complete elastic tensor within and near the skyrmion phase of MnSi. Obtaining the full elastic tensor enables direct comparison of the relation between compression and shear moduli to understand the coupling of the SKX to the underlying crystalline lattice. The thermodynamic susceptibilities measured by RUS inform measurements obtained under dynamic conditions and suggest the presence of a previously undetected intermediate regime of skyrmion motion above critical current densities that are much smaller

than determined by Hall effect and SANS measurements. This new intermediate regime is likely dominated by thermally induced creep motion of skyrmions that was predicted theoretically, but not yet observed. This suggests that skyrmion motion is possible at lower current densities than previously thought, and is an important step towards skyrmion-based applications. Our results also demonstrate that ultrasound detection is a new way to study skyrmion motion, in particular for materials where changes in the THE are small. Finally, combining high-density electrical current and ultrasonic techniques will be a useful technique to study other electric field and current sensitive systems such as multiferroic and superconducting materials.

ACKNOWLEDGMENTS

We thank F. F. Balakirev for technical support, and F. Ronning and M. Garst for insightful conversations. Work at Los Alamos National Laboratory (LANL) was performed under the auspices of the U.S. Department of Energy. Research by YL, SL, DMF, ML, ND, EDB, MJ and BM was supported by LANL Directed Research and Development program. Work by JB and AM was part of the Materials Science of Actinides, an Energy Frontier Research Center funded by the U.S. DOE, Office of Science, BES under Award DE-SC0001089.

* mpzslyk@gmail.com

† maiorov@lanl.gov

- [1] Mühlbauer S (2009) Skyrmion Lattice in a Chiral Magnet. *Science* 323:915-919.
- [2] Fert A, Cros V, Sampaio J (2013) Skyrmions on the track. *Nature Nanotechnology* 8:152-156.
- [3] Müller J (2017) Magnetic skyrmions on a two-lane race-track. *New J. Phys.* 19:025002.
- [4] Blatter G, Feigelman MV, Geshkenbein VB, Larkin AI, Vinokur VM (1994) Vortices in high-temperature superconductors. *Rev. Mod. Phys.* 66(4): 1125-1388.
- [5] Jonietz F (2010) Spin Transfer Torques in MnSi at Ultralow Current Densities. *Science* 330:1648-1651.
- [6] Schulz T (2012) Emergent electrodynamics of skyrmions in a chiral magnet. *Nat. Phys.* 8:301.
- [7] Lin SZ, Reichhardt C, Batista CD, Saxena A (2013) Particle model for skyrmions in metallic chiral magnets: Dynamics, pinning, and creep. *Phys. Rev. B* 87(21):214419.
- [8] Yu XZ (2012) Skyrmion flow near room temperature in an ultralow current density. *Nat. Commun.* 3:988.
- [9] Reichhardt C, Ray D, Reichhardt CJO (2015) Collective Transport Properties of Driven Skyrmions with Random Disorder. *Phys. Rev. Lett.* 114(21):217202.
- [10] Dong L (2015) Current-driven dynamics of skyrmions stabilized in MnSi nanowires revealed by topological Hall effect. *Nat. Commun.* 6:8217.
- [11] Nii Y, Kikkawa A, Taguchi Y, Tokura Y, Iwasa Y (2014) Elastic Stiffness of a Skyrmion Crystal. *Phys. Rev. Lett.* 113(26):267203.
- [12] Kanazawa N (2016) Critical phenomena of emergent magnetic monopoles in a chiral magnet. *Nat. Commun.* 7:11622.
- [13] Petrova AE, Stishov SM (2009) Ultrasonic studies of the magnetic phase transition in MnSi. *J. Phys.: Condens. Matter* 21(19):196001.
- [14] Migliori A, Sarrao JL (1997) Resonant Ultrasound Spectroscopy: Applications to Physics, Materials Measurements, and Nondestructive Evaluation, (Wiley, New York).
- [15] Migliori A (1993) Resonant ultrasound spectroscopic techniques for measurement of the elastic moduli of solids. *Physica B* 183:1-24.
- [16] Bauer A (2010) Quantum phase transitions in single crystal $Mn_{1-x}Fe_xSi$ and $Mn_{1-x}Co_xSi$: Crystal growth, magnetization, ac susceptibility, and specific heat. *Phys. Rev. B* 82(06):064404.
- [17] Janoschek M (2013) Fluctuation induced first-order phase transition in Dzyaloshinskii-Moriya helimagnets. *Phys. Rev. B* 87(13):134407.
- [18] Brazovskii SA (1975) Phase transition of an isotropic system to a nonuniform state. *Sov. Phys. JETP* 41:85-89.
- [19] Evans D (2017) Defect dynamics and strain coupling to magnetization in the cubic helimagnet Cu_2OSeO_3 . *Phys. Rev. B* 95:094426.
- [20] Mülbauer S (2016) Kinetic small angle neutron scattering of the skyrmion lattice in MnSi. *New J. Phys.* 18:075017.
- [21] Valenzuela SO, Bekeris V (2001) Oscillatory Dynamics and Organization of the Vortex Solid in $YBa_2Cu_3O_7$ Single Crystals. *Phys. Rev. Lett.* 86(3):504.
- [22] Rucker F *et al.* Private communications.
- [23] Choi H, Lin SZ, Zhu JX (2016) Density functional theory study of skyrmion pinning by atomic defects in MnSi. *Phys. Rev. B* 93:115112.
- [24] Maiorov B (2009) Synergetic combination of different types of defect to optimize pinning landscape using BaZrO₃-doped $YBa_2Cu_3O_7$. *Nat. Mat.* 8(5):398-404.
- [25] Campbell AM, Evetts JE (2001) Critical currents in superconductors. *Adv. Phys.* 50(8):1249-1449.
- [26] Valenzuela SO, Maiorov B, Osquiguil E, Bekeris V (2002) Elastic-to-plastic crossover below the peak effect in the vortex solid of $YBa_2Cu_3O_7$ single crystals. *Phys. Rev. B* 65(06):060504.
- [27] Fobes D (2017) Versatile strain-tuning of modulated long-period magnetic structures. *Appl. Phys. Lett.* 110:192409.
- [28] Bauer A, Garst M, Pfeiderer C (2013) Specific Heat of the Skyrmion Lattice Phase and Field-Induced Tricritical Point in MnSi. *Phys. Rev. Lett.* 110(17):177207.
- [29] Stishov SM (2007) Magnetic phase transition in the itinerant helimagnet MnSi: Thermodynamic and transport properties. *Phys. Rev. B* 76(05):052405.
- [30] Bauer A, Pfeiderer C (2012) Magnetic phase diagram of MnSi inferred from magnetization and ac susceptibility. *Phys. Rev. B* 85(21):214418.
- [31] Kittel C (2005) Introduction to Solid State Physics, (Wiley, New York, 2005).
- [32] Shekhter A (2013) Bounding the pseudogap with a line of phase transitions in $YBa_2Cu_3O_{6+\delta}$ *Nature* 498:75.
- [33] Leisure RG, Willis FA (1997) Resonant ultrasound spectroscopy. *J. Phys.: Condens. Matter* 9:6001-6029.

Supporting Information:
Elasticity in the skyrmion phase unveils depinning at ultra-low current densities

Yongkang Luo^{1*}, Shizeng Lin¹, M. Leroux¹, N. Wakeham¹, D. M. Fobes¹, E. D. Bauer¹, J. B. Betts¹, A. Migliori¹,
 J. D. Thompson¹, M. Janoschek¹, and Boris Maiorov^{1†}

¹*Los Alamos National Laboratory, Los Alamos, New Mexico 87545, USA.*

In this **Supporting Information (SI)**, we provide additional energy dispersive x-ray spectroscopy (EDS), resistivity and AC susceptibility data. We also give a brief introduction of elastic moduli and details of data analysis used for RUS measurements that support the results, discussions and our conclusions given in the main text.

SI I: Sample characterization

The stoichiometric concentrations of Mn and Si of the sample were determined by EDS measurements. Figure S1(a) shows a representative EDS spectrum. The distribution maps of Mn and Si are given in Fig. S1(b) and (c), respectively. Apparently, our single crystal exhibits a slight Mn deficiency. The average mole ratio Mn:Si=0.88:1.12. This Mn deficiency plays a crucial role in reducing the helical transition T_c and SKX pinning, as discussed in main text.

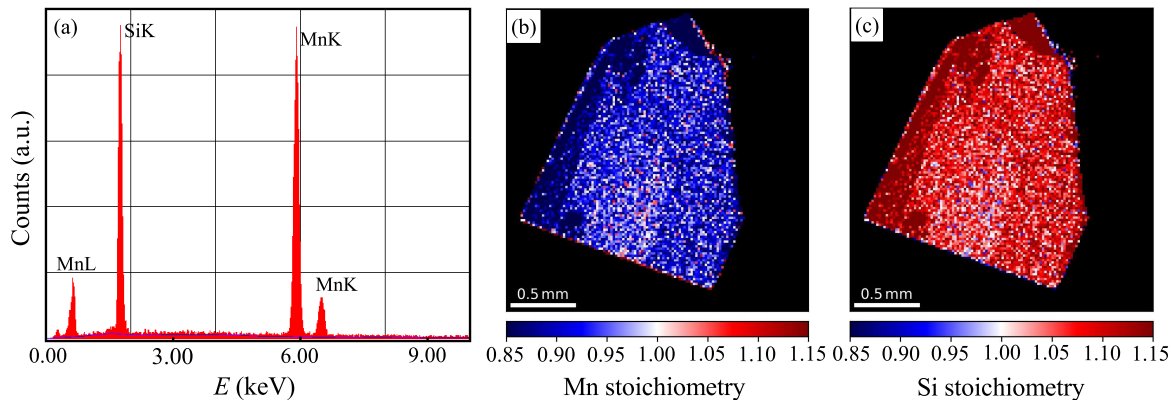


FIG. S1. (a) A representative EDS spectrum of MnSi. (b) and (c) show the maps of stoichiometric concentration of Mn and Si, respectively. The average mole ratio Mn:Si=0.88:1.12.

Figure S2(a) shows the temperature dependence of resistivity ρ measured with current applied along [100]. The resistivity decreases sub-linearly with decreasing T . Below 32 K, $\rho(T)$ starts to decrease rapidly. An inflection point is observed at 28.7 K [inset to Fig. S2(a)], used for determining $T_c=28.7$ K resistively. In the inset to Fig. S2(a), we also display $d\rho/dT$ as a function of T . A sharp peak in $d\rho/dT$ is found at T_c on top of a broad maximum which extends to ~ 32 K. Similar behavior was also seen in other thermodynamic properties[28, 29], and is a signature of pre-formed short-range HM order above T_c and a fluctuation-induced first-order transition at T_c [17].

In Fig. S2(b) we present the results of AC susceptibility measured with an alternating field $H_{ac}=3$ Oe and frequency $f=200$ Hz. When $H_{dc}=0$, $\chi'(T)$ displays a pronounced peak at T_c , consistent with resistivity and RUS measurements. For $H=1.9$ kOe, $\chi'(T)$ shows a pronounced valley between 26.8 and 28.6 K characteristic of SKX phase. This SKX phase is also seen in the isothermal $\chi'(H)$ curves shown in Fig. S2(c). These observations are akin to earlier literature[11, 30], except for the slight different field range for SKX which is probably due to a different demagnetization factor.

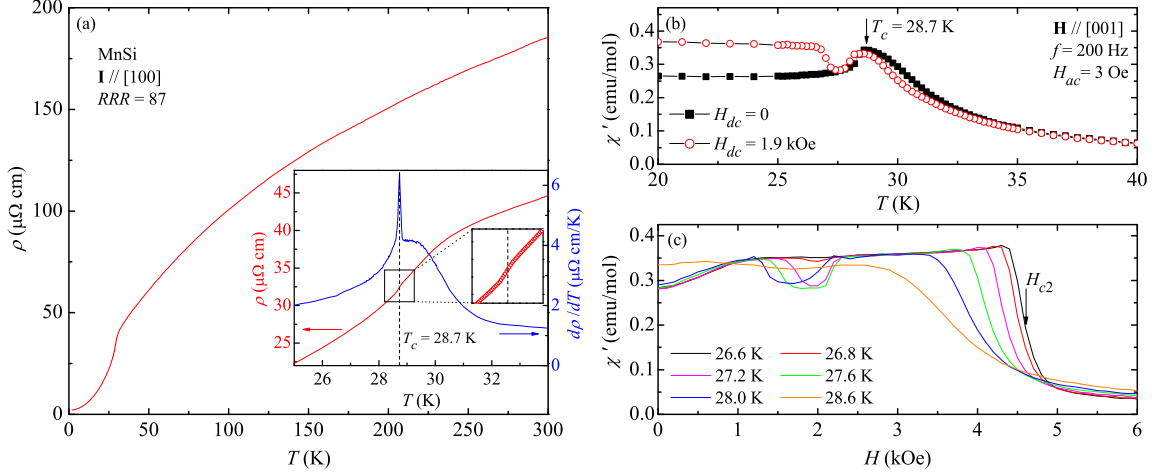


FIG. S2. (a) Temperature dependence of resistivity. The inset shows an enlarged view of $\rho(T)$ as well as $d\rho/dT$ near $T_c=28.7$ K. (b) Temperature dependent AC susceptibility χ' , measured under DC magnetic field $H=0$ (black) and 1.9 kOe (red). (c) $\chi'(H)$ measured at various temperatures. The SKX phase appears in the window $26.8 \text{ K} < T < 28.6 \text{ K}$ and between 1.5 and 2.3 kOe.

SI II: C_{ij} and problem symmetry

For a 3D crystal, we write Hooke's law as^[14, 31]

$$\boldsymbol{\sigma} = \mathbf{C} \cdot \boldsymbol{\varepsilon}, \quad (\text{S1})$$

where $\boldsymbol{\sigma}$ is the stress tensor (6×1), $\boldsymbol{\varepsilon}$ is the strain tensor (6×1), and \mathbf{C} is the elastic moduli matrix (6×6). Expanding Eq. (S1),

$$\begin{bmatrix} \sigma_1 \\ \sigma_2 \\ \sigma_3 \\ \sigma_4 \\ \sigma_5 \\ \sigma_6 \end{bmatrix} = \begin{bmatrix} C_{11} & C_{12} & C_{13} & C_{14} & C_{15} & C_{16} \\ C_{21} & C_{22} & C_{23} & C_{24} & C_{25} & C_{26} \\ C_{31} & C_{32} & C_{33} & C_{34} & C_{35} & C_{36} \\ C_{41} & C_{42} & C_{43} & C_{44} & C_{45} & C_{46} \\ C_{51} & C_{52} & C_{53} & C_{54} & C_{55} & C_{56} \\ C_{61} & C_{62} & C_{63} & C_{64} & C_{65} & C_{66} \end{bmatrix} \begin{bmatrix} \varepsilon_1 \\ \varepsilon_2 \\ \varepsilon_3 \\ \varepsilon_4 \\ \varepsilon_5 \\ \varepsilon_6 \end{bmatrix}. \quad (\text{S2})$$

Note that in this notation the subscripts 1 to 6 are actually two-element subscripts, and they correspond to the Cartesian coordinates by the following decoder table:

$$1 \leftrightarrow xx; \quad 2 \leftrightarrow yy; \quad 3 \leftrightarrow zz; \quad 4 \leftrightarrow yz, zy; \quad 5 \leftrightarrow zx, xz; \quad 6 \leftrightarrow xy, yx. \quad (\text{S3})$$

Because $C_{ij}=C_{ji}$, there are 21 different elastic moduli for an arbitrary system. The higher symmetry of the system, the lower the number of independent elastic moduli in \mathbf{C} . For cubic symmetry, \mathbf{C} becomes

$$\mathbf{C} = \begin{bmatrix} C_{11} & C_{12} & C_{12} & 0 & 0 & 0 \\ C_{12} & C_{11} & C_{12} & 0 & 0 & 0 \\ C_{12} & C_{12} & C_{11} & 0 & 0 & 0 \\ 0 & 0 & 0 & C_{44} & 0 & 0 \\ 0 & 0 & 0 & 0 & C_{44} & 0 \\ 0 & 0 & 0 & 0 & 0 & C_{44} \end{bmatrix}, \quad (\text{S4})$$

i.e., there are only three independent elastic moduli, C_{11} , C_{12} and C_{44} . This is the case for MnSi in its paramagnetic state for $H=0$. The ground state of MnSi becomes a helimagnetic order below T_c , which in principle breaks the cubic symmetry. Treating MnSi as tetragonal for $H = 0$ and $T < T_c$ is beyond the scope of this work and will be part of future efforts.

If we apply an external magnetic field $\mathbf{H}||[001]$, the principal \mathbf{z} -axis is no longer equivalent to \mathbf{x} - and \mathbf{y} -axes, the system can be regarded as tetragonal symmetry, and therefore, we have three extra elastic moduli, C_{33} , $C_{23}(=C_{31})$ and C_{66} . This situation is applicable to MnSi in the polarized paramagnetic state when a magnetic field is applied.

The skyrmion lines typically form a hexagonal lattice. An additional constraint $C^* \equiv (C_{11} - C_{12})/2 = C_{66}$ is imposed to a hexagonal symmetry, requiring now only five independent elastic moduli. This is not what we observe experimentally in Fig. 2, as $C^* \neq C_{66}$, indicating that the SKX is not setting the symmetry of the system that remains tetragonal. Furthermore, as the SKX is coupled to the crystalline lattice, this enables the observation of changes measured in the elastic moduli as shown in Fig. 2. These changes are small compared with elastic moduli from the crystalline lattice, allowing to treat the system as one with tetragonal symmetry. However, how these two lattices with different symmetries couple to each other and how to obtain a more accurate determination of the elastic moduli of SKX from the measured bulk moduli require further investigations.

The situation becomes more complicated when a DC current is applied along [100]. The current is expected to break the tetragonal symmetry into an orthorhombic one. In principle, there should be nine independent elastic moduli, C_{11} , C_{22} , C_{33} , C_{12} , C_{23} , C_{31} , C_{44} , C_{55} and C_{66} . This level of difficulty is not granted as the experimental results show that the applied current does not change the resonance frequencies or their field or temperature dependence, indicating that the symmetry of the system is not broken by low applied currents.

SI III: Data collection and analysis

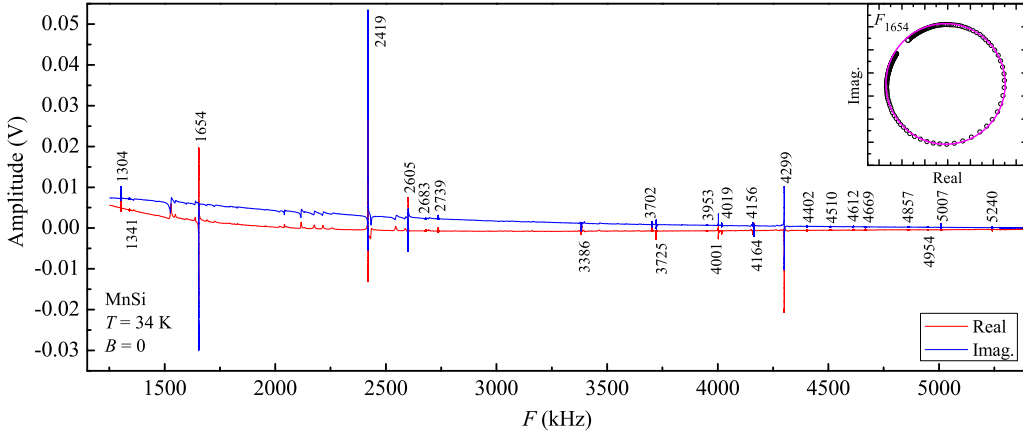


FIG. S3. Full RUS spectrum of MnSi collected at $T=34$ K in the absence of a magnetic field. The inset shows an Imaginary vs. Real plot of the resonance F_{1654} . The open symbols are experimental data, and the solid line defines a circle.

In our RUS measurement, we swept frequency from 1250 to 5300 kHz. When frequency is approaching a normal mode of the sample, a resonance is detected. We show a representative RUS spectrum of MnSi in Fig. S3 taken at $T=34$ K in the absence of magnetic field. For each resonance peak, the real part (in-phase, red) and imaginary part (out-of-phase, blue) of the signal have a Lorentzian shape $V(\omega) = z_0 + Ae^{i\phi}/(\omega - \omega_0 + i\Gamma/2)$, where Γ is the resonance width and z_0 is the background in the vicinity of the resonance. Plotting the real versus imaginary components of the resonance should form a circle in the complex plane (inset to Fig. S3). Both the width (Γ) and resonance frequency (ω_0) were obtained following an established approach[32].

For a sample with known elastic moduli, dimensions, and density, all the resonance peaks can be theoretically calculated by solving a 3D elastic wave function[14, 15, 33]. In our case, the elastic moduli are derived by a least-square-fitting, in which C_{ij} are set as free fitting parameters. The iteration continues until $\chi^2 \equiv \sum_n [(F_n^{cal} - F_n^{exp})/F_n^{exp}]^2$ minimizes, where F_n^{exp} and F_n^{cal} are the n th experimental and calculated frequencies, respectively. Table S1 shows an example of this fitting for a measurement at $T=34$ K and $H=0$ for cubic symmetry. The degree to which each resonance frequency depends on different C_{ij} , i.e. $\partial F/\partial C_{ij}$, is then calculated (normalized) and shown in the last nine columns of the table.

TABLE S1. The least-square-fitting of RUS peaks at $T=34$ K and $H=0$. The sample dimensions are $1.446 \times 0.485 \times 0.767$ mm³. The fitting derives $C_{11}=C_{22}=C_{33}=3.204192 \times 10^2$ GPa, $C_{12}=C_{23}=C_{13}=0.849543 \times 10^2$ GPa, and $C_{44}=C_{55}=C_{66}=1.263798 \times 10^2$ GPa. $\partial F/\partial C_{ij}$ (normalized) characterizes the dependencies of the fitting of a resonance peak on each C_{ij} .

n	F^{exp} (kHz)	F^{cal} (kHz)	Err (%)	$\partial F/\partial C_{ij}$								
				C_{11}	C_{22}	C_{33}	C_{23}	C_{31}	C_{12}	C_{44}	C_{55}	C_{66}
1	1304.090	1295.876	-0.63	0.95	0.03	0.04	0.02	-0.10	-0.09	0.00	0.00	0.14
2	1341.150	1338.273	-0.21	0.00	0.00	0.00	0.00	0.00	0.00	0.02	0.69	0.28
3	1654.028	1653.957	0.00	0.93	0.01	0.03	0.02	-0.08	-0.10	0.00	0.19	0.00
4	2418.830	2417.748	-0.05	1.11	0.05	0.07	0.03	-0.14	-0.11	0.00	0.00	0.00
5	2605.364	2606.384	0.04	0.10	0.01	0.01	0.00	-0.01	-0.01	0.10	0.56	0.24
6	2682.732	2688.634	0.22	0.69	0.02	0.05	0.01	-0.09	-0.05	0.00	0.00	0.37
7	2739.155	2745.038	0.21	0.31	0.02	0.01	0.00	-0.02	-0.04	0.00	0.71	0.00
8	3385.540	3380.757	-0.14	0.03	0.04	0.84	-0.08	-0.05	0.01	0.20	0.00	0.02
9	3702.542	3699.256	-0.09	0.02	0.03	0.70	-0.07	-0.03	0.00	0.16	0.06	0.12
10	3724.552	3725.367	0.02	0.26	0.01	0.03	0.00	-0.04	-0.02	0.23	0.30	0.24
11	3953.041	3986.015	0.83	0.30	0.02	0.04	0.00	-0.02	-0.04	0.00	0.70	0.00
12	4001.499	3995.519	-0.15	0.20	0.07	0.84	-0.11	-0.10	0.00	0.00	0.09	0.00
13	4018.697	4018.478	-0.01	0.34	0.02	0.04	0.01	-0.03	-0.04	0.00	0.68	0.00
14	4155.843	4140.983	-0.36	0.18	0.08	0.78	-0.11	-0.08	0.00	0.00	0.15	0.00
15	4163.504	4181.133	0.42	0.49	0.02	0.08	0.00	-0.05	-0.04	0.02	0.02	0.46
16	4299.043	4298.411	-0.01	0.58	0.00	0.74	-0.02	-0.32	0.01	0.00	0.00	0.00
17	4402.400	4379.128	-0.53	0.25	0.01	0.06	0.00	-0.05	-0.02	0.40	0.05	0.30
18	4510.335	4513.721	0.08	0.03	0.03	0.45	-0.04	-0.01	0.00	0.09	0.14	0.32
19	4612.002	4609.303	-0.06	0.02	0.15	1.04	-0.19	-0.02	0.00	0.00	0.00	0.00
20	4669.281	4648.204	-0.45	0.03	0.01	0.07	0.00	-0.01	0.00	0.52	0.08	0.31
21	4856.554	4854.090	-0.05	0.00	0.01	0.13	-0.01	0.00	0.00	0.86	0.00	0.00
22	4953.862	4960.544	0.13	0.12	0.01	0.02	0.00	-0.02	0.00	0.00	0.01	0.88
23	5007.325	5020.570	0.26	0.74	0.25	0.19	-0.09	0.11	-0.20	0.00	0.00	0.00
24	5240.128	5251.871	0.22	0.49	0.07	0.58	-0.05	-0.17	-0.03	0.00	0.11	0.00